Influence of image segmentation on one-dimensional fluid dynamics predictions in the mouse pulmonary arteries

Mitchel J. Colebank[1], L. Mihaela Paun[2], M. Umar Qureshi[1], Naomi Chesler[3], Dirk Husmeier[2], Mette S. Olufsen[1], Laura Ellwein Fix[4*]

[1]*Mathematics, NC State University, Raleigh, NC 27695, USA*

[2]*Mathematics and Statistics, University of Glasgow, Glasgow G12 8SQ, UK*

[3]*Biomedical Engineering, University of Wisconsin-Madison, Madison, WI 53706, USA*

[4]*Mathematics and Applied Mathematics, Virginia Commonwealth University, Richmond, VA 23220, USA*

[*]**Corresponding author**

Laura Ellwein Fix

Department of Mathematics and Applied Mathematics

Virginia Commonwealth University

1015 Floyd Ave.

Richmond, VA 23220

Email: lellwein@vcu.edu

Phone: 804-828-2748

Fax: 804-828-8785

Abstract

Computational fluid dynamics (CFD) models are emerging tools for assisting in diagnostic assessment of cardiovascular disease. Recent advances in image segmentation has made subject-specific modelling of the cardiovascular system a feasible task, which is particularly important in the case of pulmonary hypertension (PH), requiring a combination of invasive and non-invasive procedures for diagnosis. Uncertainty in image segmentation propagate to CFD model predictions, making quantification of segmentation induced uncertainty crucial for subject-specific models. This study quantifies the variability of one-dimensional (1D) CFD predictions by propagating the uncertainty of network geometry and connectivity to blood pressure and flow predictions. We analyse multiple segmentations of a single, excised mouse lung using different pre-segmentation parameters. A custom algorithm extracts vessel length, vessel radii, and network connectivity for each segmented pulmonary network. Probability density functions are computed for vessel radius and length and then sampled to propagate uncertainties to haemodynamic predictions in a fixed network. In addition, we compute the uncertainty of model predictions to changes in network size and connectivity. Results show that variation in network connectivity is a larger contributor to haemodynamic uncertainty than vessel radius and length.

Keywords: Haemodynamics, fluid dynamics, pulmonary circulation, uncertainty quantification, image segmentation

1 Introduction

Definitive diagnosis of pulmonary hypertension (PH), defined as a mean pulmonary arterial blood pressure $\geq$ 25 mmHg, requires a series of medical tests including invasive right heart catheterization and non-invasive computed topography (CT) imaging of the heart and lungs (1). Diagnostic protocols interpret each data source independently to make an ultimate decision about disease classification and severity (2), but recent studies (3,4) have proposed assimilation of haemodynamics and imaging data with computational fluid dynamics (CFD) modelling, providing insight into the structure and function of the pulmonary system.

Medical imaging and image segmentation have emerged as powerful non-invasive tools for disease diagnostics (5-7), providing an abundance of data for analysing the structure and function of the cardiovascular system under physiological and pathological conditions (1). Advances in image segmentation include semi- and fully-automated algorithms for geometric reconstruction of complex vascular regions (8,9). However, inherent uncertainty is present as most image segmentation software require manual specification of the image intensity thresholds (pre-segmentation parameters) between background and foreground. For example, van Horssen et. al (10) showed that variation in image

resolution affected the cumulative volume of a cast of the coronary arterial tree after segmentation. Rempfler et. al (11) compared segmentation algorithms on retinal images, showing that posterior probability estimates for foreground pixels varied with different segmentation techniques when compared to the true segmentation or so-called "ground-truth". In contrast to the aforementioned studies, *in-vivo* images are only captured up to a finite resolution, which makes ground-truth rendering impossible. These two studies quantified variability in segmented networks but did not investigate how this uncertainty affected pulsatile haemodynamics.

Haemodynamic predictions (*e.g.,* cross-sectional averaged flow and pressure) in the pulmonary vasculature are often computed using either three-dimensional (3D) (12) or one-dimensional (1D) (3) CFD models. 3D models predict local flow patterns with more precision (4) but are computationally expensive, making it difficult to perform multiple forward model evaluations for uncertainty quantification, i.e. UQ (13). For instance, Sankaran et. al (14) computed 3D CFD model sensitivity to coronary stenosis diameters, using surrogate model approximations to combat high computational cost. However, they did not account for possible changes in network connectivity nor for the uncertainty from the initial segmentations of the vasculature. In contrast, 1D models are more computationally efficient, reducing the need for surrogates and allowing for investigations into variability of network connectivity. Moreover, a recent study (15) of the coronary vasculature showed that 1D models attain similar haemodynamic predictions as 3D when using appropriate boundary conditions. Recent studies analysed 1D systemic arterial models (10,16) to understand how uncertainty in network structure impacts haemodynamics. Fossan et. al (17) devised an optimization strategy to determine the number of vessels needed to match haemodynamic predictions in the coronary arteries, and Huberts et al. (13) used polynomial chaos expansion to quantify the sensitivity of flow predictions to variations in vessel radius. In contrast to the systemic circulation, the pulmonary vasculature is more compliant, branches more rapidly, and operates at a much lower mean pressure, indicating that results from the systemic circulation may not be valid for comparison.

The total uncertainty in the haemodynamic prediction is a combination of uncertainty in the model parameters and uncertainty from the modelling framework. As noted above, several previous studies have studied uncertainty with respect to prescribed haemodynamic parameters and the 1D approximation, but to our knowledge this is the first known investigation of the impact of uncertainties in network reconstruction on CFD simulations in the pulmonary vasculature. Specifically, our study examines how pre-segmentation parameters impact estimated vessel radius, vessel length, and network connectivity, and propagate this uncertainty to haemodynamic predictions in the pulmonary circulation. To do so, we analyse multiple segmentations of a microcomputed tomography (micro-CT) image from a mouse pulmonary arterial tree. We propagate this uncertainty using a 1D CFD model by constructing the model domain from each

segmentation. Inverse UQ is performed by estimating probability density functions (PDFs) for vessel radii and length, and then propagating uncertainties (forward UQ) using Monte Carlo sampling. Uncertainty in haemodynamic predictions is quantified by analysing three sets of predictions (depicted in figure 1); 1) predictions using 25 segmented networks (*total variation*); 2) predictions from a representative network with fixed connectivity when drawing realizations of length and radius perturbations (*parameter variation*); and 3) predictions from the same representative network when geometric parameters are fixed, but connectivity and network size are varied (*network variation)*. We argue that UQ is an essential component of the model analysis when computational models are integrated into clinical protocols. The animal dataset used here (18,19) serves as a preliminary step in understanding disease progression and has potential for extrapolation to human PH.

FIGURE_1_WORKFLOW

Figure 1: Workflow for uncertainty quantification of haemodynamics. Multiple segmentations are performed to construct the segmented networks (SNs), of which one network is selected as the represented network (RN). Inverse uncertainty quantification (UQ) is performed on the 25 SNs by estimating probability density functions (PDFs) for vessel radius and length. The 25 SNs are used in model simulations to understand the total variation, while the PDFs for the vessel dimensions are used to propagate uncertainty in the parameter variation study. Lastly, we change the structure of the RN to understand the variation induced by network connectivity. Pressure and flow predictions are then compared from the three sources of variation.

2. Materials and methods

2.1 Experimental data

This study uses existing micro-CT and haemodynamic data from two male C57BL6/J control mice aged 10-12 weeks. A detailed description of experimental protocols for the imaging and haemodynamic data can be found in Vanderpool et. al (18) and Tabima et. al (19), respectively. Briefly, haemodynamic data includes a flow waveform ensembled over 20 cardiac cycles measured using an in-line flow meter (Transonic Systems, Ithaca, NY) in the main pulmonary artery (MPA). The imaging data is obtained after euthanisation and inflation of the mouse lung at 17.2 mmHg. A cannula with outer diameter 0.127 cm and inner diameter of 0.086 cm is attached to the MPA before 360-degree imaging and reconstruction to DICOM 3.0 files. Both procedures were approved by the University of Wisconsin-Madison Institutional Animal Care and Use Committee.

FIGURE_2_ITK-SNAP

Figure 2: ITK-SNAP interface for prescribing (θ_1,θ_2). Voxel intensities in the histogram are mapped to foreground and background based on thresholding function (red curve) and pre-segmentation parameters. Here, we only assume a lower threshold on image intensities, as shown by the constant value of 1 in the threshold function for all values greater than the lower threshold.

2.2 Image analysis

2.2.1 Image segmentation

The micro-CT image is stored as a DICOM 3.0 file with voxel dimensions $497 \times 497 \times 497$. The gray-scale image (shown in figure 4a) is transformed to a binary map identifying the vascular ("foreground") and non-vascular ("background") regions using global thresholding and image segmentation in ITK-SNAP (20). Global thresholding is a pre-segmentation technique requiring a priori selection of thresholds to specify the image intensity bounds of the foreground. Threshold bounds are traditionally selected in an *ad hoc* manner to ensure that the foreground is captured (3,21,22). In addition, ITK-SNAP requires specification of a smoothing parameter to determine the boundary between the foreground and background (see figure 2). Due to the experimental protocol and use of perfused contrast, the image segmented in this study does not contain high intensity voxels from other anatomical features (*e.g.,* the veins or the heart) within the region of interest. Therefore, only the lower threshold (θ_1) and smoothing (θ_2) pre-segmentation parameters require specification.

Acceptable intervals for (θ_1,θ_2) are determined to preserve the foreground for the large vessels across segmentations. To study segmentation induced uncertainty, we assume a uniform distribution for the two parameters, with $20 \leq \theta_1 \leq 45$ and $3 \leq \theta_2 \leq 8$, and draw 25 realisations of pre-segmentation parameter sets (θ_1,θ_2) (given in table 1) using the *rand* function in MATLAB (Mathworks, Natick, MA). As shown in figure 3, the foreground for distal vascular segments changes significantly when (θ_1,θ_2) are varied, but maintains features for the large, proximal vessels.

We use active contour evolution, a semi-automated segmentation algorithm available in ITK-SNAP, to segment the micro-CT image (see the supplement, §S.1). We consistently use 2000 iterations of the contour evolution, ensuring that the largest arteries carrying the majority of the blood volume are captured. The imaging protocol described in Vanderpool et. al (18) has a spatial resolution between 30-40 μm, providing a lower bound of 40μm for the measurement uncertainty diameter (20μm for radius).

FIGURE_3_FOREGROUND

Figure 3: Qualitative differences in foreground (white) of distal vascular segments when changing the lower threshold (θ_1) and the smoothing parameter (θ_2). Top: changes in foreground with θ_1; bottom: changes in foreground with θ_2.

FIGURE_4_NETWORK

Figure 4: Image to network workflow. a) the foreground visible in the image file; b) the 3D rendering of the vascular foreground; c) centerlines obtained using VMTK; d) a graph representation of the network used in the 1D model with vessels (edges) and bifurcations (nodes) identified using custom MATLAB algorithms.

2.2.2 Network reconstruction

Segmented geometries are exported as surface meshes and converted to VTK polygonal files using Paraview (23) (Kitware, Clifton Park, NY). Surface mesh VTK files were imported into VMTK (www.vmtk.org) (6) to extract vessel segment centerlines, lengths, and radii using native scripts. We developed a custom MATLAB algorithm to extract the network connectivity from the extracted quantities and identify all the vessels in each network. Subsequently, we use a recursive algorithm to construct a connectivity matrix identifying the geometry of the tree used in the 1D model. Further details of the reconstruction are given in the supplement, §S.2. Figure 4 illustrates the workflow starting from the micro-CT image segmentation and ending with the connected network representation.

Voxels are converted to cm using a scaling factor based on the known diameter of the cannula (0.086 cm). The MPA radius is estimated using measurements distal to the cannula before the left (LPA) and right (RPA) pulmonary arterial bifurcation. Figure 5 shows an example network with radii estimates at each point along the network and within a single vessel. Measured values for radii vary within each vessel segment, limiting our inference of tapering. To proceed with calculations, we fix the vessel radius to be the mean over the centre 80% of the individual estimates, which mitigates the impact of extreme diameters in the ostium regions at either end of each segment.

We construct connected graphs using the centreline data and create a connectivity matrix linking vessels, represented by their length and radius, and bifurcations. In addition, we capture global network features including the number of vessels, the number of bifurcations (*i.e.* generations), and the total

vascular volume. The CFD model used for haemodynamics modelling assumes a binary structure, with each generation of the tree being formed by a new set of vessels. The resulting networks were found to have no loops within the region of interest studied here. To characterize branching properties, we compute morphometric indices for each network including structured tree scaling parameters, asymmetry and area ratios, and Murray's exponent (see the supplement, §S.7 for details).

FIGURE_5_COMPONENTS

Figure 5: Components of an arterial tree. a) 3D segmentation of network; b) centerline representation of a tree with the 32 vessel-subset (red and blue); c) magnification of the representative vessel in blue from panel (b) depicting radius estimates; d) radius estimates along the representative vessel in panel (c), where the center 80% of points are used to calculate the mean radius. Actual radius values obtained in (d) are calculated at orthogonal centerline slices in VMTK, while panel (c) shows non-orthogonal radii estimates for illustrative purposes.

2.3 Haemodynamics modelling

2.3.1 Blood flow model.

Similar to previous studies (3,24,25), we use a 1D CFD model to predict time-varying flow, pressure, and area in each vessel. The model is derived under the assumptions that vessels are cylindrical, blood is incompressible, and flow is laminar, axisymmetric, and Newtonian. The model equations are obtained by integrating over the cross-sectional area of the vessel, described in detail in (3). Mass conservation and momentum balance are then given by

$$\frac{\partial A}{\partial t} + \frac{\partial Q}{\partial x} = 0, \tag{2.1}$$

$$\frac{\partial Q}{\partial t} + \frac{\partial}{\partial x}\left(\frac{Q^2}{A}\right) + \frac{A\partial P}{\rho \partial x} = -\frac{2\pi\nu R Q}{\delta \quad A}, \tag{2.2}$$

where x (cm) and t (s) denote the axial and temporal coordinates, $A(x,t)$ (cm^2) denotes the cross-sectional area, $Q(x,t)$ (cm^3/s) the volumetric flow rate, $P(x,t)$ (mmHg) is the transmural blood pressure, and $R(x,t)$ (cm) the vessel radius. The blood density $\rho = 1.057$ (g/cm^3) and the kinematic viscosity $\nu = 0.0462$

(cm²/s) are assumed constant (26,27). The right-hand side of equation (2.2) accounts for the frictional losses by assuming a flat velocity profile

$$u = \begin{cases} \overline{u} & \text{for } r \leq R - \delta \\ \overline{u}(R - r)/\delta & \text{for } R - \delta \leq r \leq R \end{cases} \tag{2.3}$$

with a linearly decreasing boundary layer with thickness $\delta = \sqrt{\nu T / 2\pi}$ (cm), where T(s) is the length of the cardiac cycle extracted from data (3,28). To close the system of equations, we consider a constitutive law relating blood pressure and vessel cross-sectional area. We model vessels as thin walled, incompressible, homogeneous, and orthotropic cylinders tethered in the longitudinal direction. Under these conditions, the linear stress-strain relation (3,29,30) is given by

$$P - P_0 = \frac{4}{3}\beta\left(1 - \sqrt{\frac{A_0}{A}}\right), \tag{2.4}$$

where $\beta = Eh/r_0 = 37.5$ mmHg describes the arterial stiffness, E (mmHg) is the Young's modulus in the circumferential direction, h (cm) the wall thickness, and $A_0 = \pi r_0^2$ (cm²) is the reference area obtained at the reference pressure P_0 (mmHg).

The system (2.1) - (2.4) is solved using the two-step Lax-Wendroff finite difference scheme in C++ (24) with a temporal resolution of 1.3×10^{-5}(s) and a spatial resolution of 0.025 (cm) ensuring that the Courant-Fredrich-Lewy (CFL) condition is not violated. To ensure stability and convergence of the numerical scheme, the lengths of any vessels shorter than the spatial resolution of the solver are artificially augmented to be the size of two grid points.

2.3.2 Wave intensity analysis

Wave propagation in the pulmonary system can be characterized using wave intensity (WI) analysis (31). Detailed derivations of WI quantities can be found in the supplement, §S.3. Briefly, considering $Q = AU$, where U is the blood flow velocity (m/s) in the vessel under the assumption of negligible frictional losses, we define the forward and backward components of WI as

$$WI_{\pm} = (\delta P_{\pm}/\delta t)(\delta U_{\pm}/\delta t), \tag{2.5}$$

Where '+' and '-' indicate the direction of the local waves, and $\delta P_{\pm}$ and $\delta U_{\pm}$ are the associated pressure and velocity "wavefronts", (3,32). The wave separation depends on the local pulse wave velocity (PWV)

$$c(P) = \sqrt{\frac{A\partial P}{\rho \partial A}}. \tag{2.6}$$

Local waves can either be compressive or decompressive (28,31). Wave reflections are current clinical indicators for pulmonary vascular disease and PH progression and can be attributed to impedance mismatch at both proximal and distal vessel junctions (31,32).

2.3.3 Inflow, outflow and junction conditions

The system governed by equations (2.1) - (2.4) is hyperbolic with characteristics pointing in opposite directions, thus two boundary conditions are needed at each vessel inlet and outlet. At the network inlet (the MPA) we prescribe a measured flow waveform from a single cardiac cycle. At network bifurcations we impose two conditions ensuring conservation of flow and a continuity of pressure,

$$Q_p(l_p,t) = Q_{d_1}(0,t) + Q_{d_2}(0,t), \qquad P_p(l_p,t) = P_{d_1}(0,t) = P_{d_2}(0,t), \tag{2.7}$$

where the subscripts p, d_1, d_2 indicate the parent and daughter vessels and l_p denotes the length of the parent vessel. Lastly, we impose a three element Windkessel model at the outlet of terminal vessels (4) to characterize the downstream vasculature, which relates pressure and flow via an RCR circuit model

$$\frac{dP(l,t)}{dt} = R_1\frac{dQ(l,t)}{dt} + Q(l,t)\left(\frac{R_1+R_2}{R_1R_2}\right) - \frac{P(l,t)}{R_2C_T} \tag{2.8}$$

where R_1 is the proximal resistance, R_2 is the distal resistance, and C_T is the total compliance (29,33).

2.3.4 Parameterization

The haemodynamics modelling parameters include those describing the vascular structure (radius, length, and stiffness), the fluid dynamics (including viscosity, density, and the boundary layer thickness), and the inflow and outflow boundary conditions. We assume that inflow, viscosity, density, and wall stiffness (β) are fixed and independent of the network geometry (3,28,34), while parameters specifying the vessel radius, length, and Windkessel outflow boundary conditions (R_1, R_2, C_T) depend on the network structure (3,17).

For each network, vessel radii and length are determined from the segmentation, while estimates are needed for Windkessel parameters. Similar to our previous study (3), we assume that the total compliance C_T can be determined from the diastolic decay time constant $\tau = R_TC_T$, where $R_T = R_1 + R_2$ is the total vascular resistance (3). R_T is computed as the ratio of mean pressure to mean flow, *i.e.* $R_T = \overline{P}/\overline{Q}$, and as discussed in our previous studies (3,30), *a priori* resistance values for each terminal vessel can be calculated using Poiseuille's equation, relating mean pressure and flow via the vessel dimensions. Both junction conditions in equation (2.7) are used together with Poiseuille's law to give the mean flow distribution relationship

$$\overline{Q}_{d_1} = \overline{Q}_p \frac{\xi_{d_1}}{\xi_{d_1} + \xi_{d_2}}, \quad \text{and} \quad \overline{Q}_{d_2} = \overline{Q}_p \frac{\xi_{d_2}}{\xi_{d_1} + \xi_{d_1}}, \tag{2.9}$$

where $\xi_i = r_i^4 / l_i$, consistent with Poiseuille's equation (see the supplement, §S.4 for details). Finally, we set $R_1 = 0.2R_T$ and $R_2 = 0.8R_T$ (3,30).

2.4 Inverse uncertainty quantification

We employ inverse UQ to estimate vessel length and radius PDFs over the 25 segmented networks. To compare measurements across segmentations, PDFs are computed for radius and length from a 32-vessel subset after data standardization. Two estimation techniques, kernel density estimation (KDE) and Gaussian process (GP) density estimation, are used to compare estimated PDFs. Weighted least squares regression and GP regression are used to remedy the issues of non-constant variance, *i.e.* heteroscedasticity, in vessel dimensions.

2.4.1 Data standardization

A subset of 32 pulmonary vessels of various calibre (see figure 5b) is selected from the 25 segmented networks. The 32 vessels are visible in all 25 networks and contain radius and length measurements that encompass the full range of measurements in the networks. Length and radius measurements are standardized using

$$s_{i,j}^* = \frac{s_{i,j} - \overline{s}_i}{\sigma_{s_i}}, \tag{2.10}$$

where $s_{i,j}$, $s = r,l$ are the measured quantities from the ith vessel and jth segmentation, and $\overline{s}_i$ and σ_{s_i} are the mean and the standard deviations of these quantities across the 25 networks.

2.4.2 Density estimation

KDE, a nonparametric technique (35), estimates the PDFs for radius and length. This technique requires specification of a bandwidth parameter, determining how influential each data point is in the density estimation. We consider both Silverman's rule of thumb (35) and maximum likelihood leave-one-out cross validation (36) for bandwidth estimation. These methods are compared to logistic GP density estimation (37) using the *GP Stuff* toolkit in MATLAB (38). Due to space restrictions, the methodological details have been relegated to the supplementary material, §S.5.

2.4.3 Statistical models for computing the length and radius variance

The PDFs constructed from the 32-vessel subset are representative of the overall variation in the length and radius across all the segmented networks. However, the magnitude of σ_{l_i} and σ_{r_i} vary from vessel to

vessel and need to be modeled explicitly before forward UQ. We use the coefficient of variation, $c_v^{s_i} = \sigma_{s_i} / \bar{s}_i$ to compare these measurements' variability.

The statistical model $\phi(\bar{s}_i) = c_v^{s_i}$ relates the average measurements of radius and length across segmentations to their coefficient of variation. The variance of the measurements exhibits heteroscedasticity, as smaller vessel segments are more sensitive to pre-segmentation parameters leading to non-constant variance. This violates the assumptions of ordinary linear regression; hence we consider weighted least squares regression and GP regression with input-dependent noise (39). Deterministic weighted least squares regression iteratively fits regression models by updating weights for each data point. The optimal weights (optimal in a maximum likelihood sense) are given by the inverse of the variance of the response $\phi(s_i)$ (40). Since this variance is unknown, we approximate the weights as $1/\epsilon_i^2$, where ϵ_i is the residual from the unweighted regression model, reducing the impact of highly variable observations on the regression prediction. We consider exponential, logarithmic, square root, and linear weighted least squares regression models. For GP regression, we employ a GP for the response, $c_v^{s_i}$, and for the latent variance of $c_v^{s_i}$. We use the Matérn covariance function (41) with a smoothness parameter $\nu = 5/2$ in the GP formulation (see the supplement, §S.6 for more details).

2.5 Forward Uncertainty Quantification

Forward UQ propagates model and parameter uncertainties to simulated quantities of interest. To analyse the posterior variation in model predictions, we pursue three sets of simulations determining (i) the total variation of haemodynamic predictions associated with segmentation, (ii) the variation to changes in vessel radius and length, and (iii) the variation to changes in network size and connectivity. The first set of simulations (i) use the 25 segmented networks, whereas the last two (ii-iii) are conducted in a representative network.

2.5.1 Total variation

We predict haemodynamics using each of the 25 segmented networks to quantify the total variation of flow and pressure predictions in the MPA, LPA, and RPA. The observed variation is attributed to several sources of uncertainty, including the parameters of the model and the size and connectivity of the network. Once the total variation is calculated, we quantify the relative contributions from the parameter and network variation.

2.5.2 Representative network

A representative network is used to examine the variation in vessel radius and length and changes in network size and connectivity. We first compute the MPA pressure waveform for each of the 25

segmented networks, then we ensemble average these to determine a mean MPA pressure. The network with the smallest least squares cost between its MPA pressure waveform and the ensemble averaged waveform is designated as the representative network.

2.5.3 Parameter variation

As mentioned in §2.3, we assume that density, viscosity, and vessel stiffness are constant while parameters impacted by image segmentation, including vessel length and radius, vary. The outflow boundary conditions are dependent on vessel length and radius; thereby, we analyse the variation in model predictions associated with changes in vessel dimensions.

We compute inverse cumulative distribution functions (CDFs) for the length and radius PDFs. The inverse CDF, $F_s^{-1}(\alpha)$, is a nondecreasing function defined on the interval $[0, 1]$ that provides values from the original PDF, allowing for inverse transform sampling for forward UQ (13). Briefly, let u be a realization from a uniform distribution, $u \sim \mathcal{U}(0,1)$, and define the realization from the inverse CDF as $F_s^{-1}(u)$. There exists a mapping from the realization to the inverse CDF for the radius and the length via $\gamma_r = F_r^{-1}(u)$ and $\gamma_l = F_l^{-1}(u)$, hence we draw samples from the inverse CDF to provide standardized measurements l^* and r^* for length and radius.

We define a mapping from the inverse CDF of $\bar{s}_i$ in vessel i to the perturbed values $\hat{s}_i$ (in units of cm). Writing $F_s^{-1}(u) = (\hat{s}_i - \bar{s}_i)/\sigma_{s_i}$ and $\sigma_{s_i} = c_v^{s_i} \cdot \bar{s}_i = \phi(\bar{s}_i) \cdot \bar{s}_i$, where $\phi(\bar{s}_i)$ is the statistical model found from §2.4.3, we get

$$\hat{s}_i = \left(F_s^{-1}(u) \cdot \phi(\bar{s}_i) + 1\right) \cdot \bar{s}_i \tag{2.11}$$

for each average measurement $\bar{s}_i$ in vessel i. The values $\hat{s}$ are used as the dimensions for each vessel in the 1D model when doing the forward UQ. We set $\bar{s}_i = s_i^{rep}$, where s_i^{rep} are the original measurements from the representative network. To ensure convergence of the posterior predictions (29), we draw $M = 10^4$ realizations using Monte Carlo sampling. The pseudo algorithm for UQ propagation is as follows:

1. Draw a random sample $u \sim \mathcal{U}(0,1)$.
2. Map the sample to $F_r^{-1}(u)$ and $F_l^{-1}(u)$.
3. Perturb the nominal radius and length by using equation (2.11).
4. Run 1D CFD model with new radius and length values.
5. Repeat steps 1-4 M times.

2.5.4 Network variation

We simulate the effect of network truncation by iteratively eliminating terminal vessel pairs from the representative network. To do so, we calculate the total volume of each terminal vessel (i.e. $V_{tot} = \pi r^2 l$)

and remove vessels with the smallest volume. Total resistance, total compliance and total mean flow in the network are conserved during this process, the details of which are in the supplementary material, §S.3.

3 Results

We analyse the total variation of flow and pressure predictions and identify the relative contributions from variations in vessel parameters and in the network. Variation in model predictions is quantified by comparing simulations in the MPA, LPA, and RPA.

3.1 Network statistics

Figure 6 summarizes network characteristics obtained from the 25 segmented networks, including number of vessels (panel a), average cross-sectional area (panel b) and total cross-sectional area (panel c) in each generation. The average number of vessels across the networks is 437 with a standard deviation of 76 and the mean number of generations across segmentations is approximately 17. The number of vessels and total cross-sectional area of the networks are consistent across segmentations up until the 6^{th} generation, after which the results deviate. Most segmentations achieve a maximum number of vessels and cross-sectional area between generations 8 and 14, while the average cross-sectional area rapidly decreases until the 5^{th} generation, and then remain fairly constant afterward. Analysis across all networks in panel d shows that one network (corresponding to $(\theta_1,\theta_2) = (44, 7.6)$) is an outlier, having significantly fewer vessels and a lower total cross-sectional area. Table 1 includes all pre-segmentation parameter sets used in the repeated segmentations as well as network level features. Results of calculating morphometric indices show that the parent to daughter area ratio is greater than 1 and that Murray's exponent is approximately 3 (see supplement §S.7), consistent with literature findings (30,43).

3.2 Inverse UQ

Table 1. *Summary of pre-segmentation parameters and network features*

Figure 7 shows the length and radii KDE for the 32 representative vessels computed using Silverman's rule, maximum likelihood cross validation, and GPs. Before density estimation, the standard deviation for each of the 32 vessels is used to normalize the data (see equation (2.7)). The maximum coefficient of

FIGURE_6_FEATURES

Figure 6: Morphometric features from the 25 segmentations marked by different colored lines. The number of vessels (a) is consistent between segmentations until the 5th generation. The average cross-sectional area (b) decreases rapidly after the 1st generation, while the total cross-sectional area (c) varies significantly between segmentations. The segmentation parameters are plotted against each other in (d), with a clear outlier present at $(44, 7.6)$ (in pink) indicating a set of pre-segmentation parameters that have marked effects on the network structure. The outlier has lower number of vessels and total cross-sectional area as depicted in the pink curve in panels (a) and (c).

Pre-segmentation parameters (θ_1, θ_2)	Number of vessels	Number of generations	Number of terminal vessels	Total volume (cm^3)
(22, 5.0)	276	15	149	21.0871
(25, 6.0)	422	17	226	21.3407
(26, 4.7)	415	17	219	22.3524
(26, 4.8)	425	18	227	22.8591
(26, 5.1)	441	17	234	22.7031
(27, 5.8)	450	17	240	22.9599
(28, 6.0)	333	15	178	20.6542
(30, 4.6)	428	16	230	21.7283
(30, 5.7)	461	17	245	23.0039
(30, 6.5)	476	18	252	23.1922
(30, 8.0)	409	16	220	21.7642
(31, 5.6)	462	18	246	23.3346
(31, 6.1)	310	15	164	18.2311
(32, 4.1)	419	16	220	22.2851
(33, 4.2)	446	18	239	23.0664
(33, 5.1)	505	18	269	24.6089

variation is 21% for the radius and 49% for the length estimate. The bandwidth estimates for Silverman's

(34, 3.3)	495	18	265	24.1804
(34, 3.4)	474	17	257	24.2923
(35, 3.6)	459	17	242	23.2488
(35, 4.8)	470	17	250	23.0868
(35, 6.8)	404	17	214	22.7536
(36, 4.0)	419	17	226	22.0391
(36, 4.1)	376	16	197	22.5833
(37, 3.9)	409	17	221	21.6596
(44, 7.6)	185	12	98	20.4368

FIGURE_7_ESTIMATES

Figure 7: Density estimates (a) and (b) and inverse cumulative distribution functions (c) and (d) for the standardized radius and length values, respectively, measured in the 32-vessel subset. The bandwidth parameters used for the length and radius KDEs were determined using Silverman's rule (blue, dash dot) and maximum likelihood cross-validation (MLCV, red, dashed). The Gaussian process (GP) mean and 95% confidence interval are shown as a solid curve with grey bands. Standardized values are denoted by the black tick marks in panels (a) and (b).

rule are $\mathrm{H_l^S} = 2.038 \times 10^{-1}$ and $\mathrm{H_r^S} = 1.573 \times 10^{-1}$, while for the maximum likelihood cross validation the estimated bandwidths are $\mathrm{H_l^{MLCV}} = 1.808$ and $\mathrm{H_r^{MLCV}} = 6.887 \times 10^{-1}$ for the length and radius densities, respectively. Computations using Silverman's rule exhibit overfitting, while the maximum likelihood cross validation over-smooths the density relative to the GP. In summary, the GP density estimation provides the most robust approximation for the KDE, which is therefore chosen in the forward uncertainty propagation in §3.3.

Weighted least squares with exponential, logarithmic, square root, and linear regression functions are unable to resolve the heteroscedastic nature of the data (plots not shown). Instead, we use the GP regression model with input dependent noise to estimate $\phi(\bar{s}_i)$, resolving the issue of heteroscedasticity. Figure 8 panels (a) and (b) show the GP regression for $c_v^{r_i}$ and $c_v^{l_i}$, respectively, while panels (c) and (d) depict the latent variance. The coefficient of variation for vessel measurements across segmentations increases as vessels get smaller. The mean variance for c_v^l increases as the length decreases, yet the mean variance of c_v^r has a sharp decrease for the smallest vessels. Both GP models stay above the minimum variability of $20\mu m$.

FIGURE_8_GP

Figure 8: Gaussian Process (GP) regression using non-constant variance for the relationship between length and radius and their coefficient of variation (c_v). The GP means and standard deviations are computed from the c_v data obtained from the 32-vessel subset (asterisks) and plotted against the analytical bound of the image resolution (blue, dash-dot curve). The mean of the GPs and $\pm$ one and two standard deviations (SD) from the mean are shown in (a) and (b) in black, dark grey, and light grey, respectively. The variance of the GPs in (c) and (d) are predicted using an additional GP and provide a mean (black) and variance (dashed curve) for the variance estimate. Both mean curves in (a) and (b) are above the uncertainty bound of the imaging protocol.

FIGURE_9_PREDICTIONS

Figure 9. Pressure and flow predictions in the first pulmonary bifurcation when studying total variation, parameter variation, and network variation. Predictions from the total variation include simulations in the 25 segmented networks, the representative network (in red), and $\pm$ 2 s.d. from the mean (blue, dash-dot). The parameter variation plots (2nd column) show the 10,000 Monte Carlo realizations (grey) along with the mean (black) $\pm$ 2 s.d. from the mean (blue, dash-dot). Lastly, the network variation predictions (3rd column) show the predictions when using 219 vessels in the network (bright red) up until the network is reduced to the MPA, LPA, and RPA (black).

FIGURE_10_WI

Figure 10. Wave intensity (WI) analysis in the first pulmonary bifurcation. Forward (positive values) and backward (negative values) waves are calculated for the total variation and parameter variation (grey lines) along with $\pm$ 2 s.d. from the mean (forward waves, magenta; backward waves, cyan). Predictions from the network variation study are color coded according to network size, as described in Figure 9.

Table 2. *Results from simulations*

Pressure				
Total variation	Mean pressure	Systolic pressure	Diastolic pressure	Pulse pressure
MPA	20.36 ± 0.78	35.35 ± 1.63	10.02 ± 0.27	25.33 ± 1.39
LPA	19.66 ± 0.79	33.46 ± 1.67	10.00 ± 0.27	23.45 ± 1.43
RPA	19.52 ± 0.78	32.83 ± 1.60	10.10 ± 0.28	22.74 ± 1.34
Parameter variation	Mean pressure	Systolic pressure	Diastolic Pressure	Pulse Pressure
MPA	20.38 ± 0.54	35.37 ± 1.03	10.04 ± 0.23	25.33 ± 0.82
LPA	19.68 ± 0.53	33.46 ± 0.99	10.02 ± 0.23	23.43 ± 0.78
RPA	19.56 ± 0.50	33.46 ± 0.90	10.11 ± 0.24	22.80 ± 0.69
Network variation	Mean pressure	Systolic pressure	Diastolic Pressure	Pulse Pressure
MPA	18.29 ± 0.84	31.70 ± 2.07	9.08 ± 0.18	22.63 ± 1.91
LPA	17.44 ± 0.86	29.34 ± 2.13	9.08 ± 0.17	20.27 ± 1.97
RPA	17.31 ± 0.83	28.71 ± 1.96	9.15 ± 0.20	19.56 ± 1.77
Flow				
Total variation	Mean flow	Max Flow	Min flow	Volume
LPA	0.142 ± 0.004	0.447 ± 0.013	-0.000 ± 0.000	0.016 ± 0.000
RPA	0.027 ± 0.004	0.113 ± 0.009	-0.015 ± 0.004	0.003 ± 0.000
Parameter variation	Mean flow	Max flow	Min flow	Volume
LPA	0.140 ± 0.001	0.439 ± 0.006	0.000 ± 0.015	0.015 ± 0.000
RPA	0.029 ± 0.001	0.119 ± 0.007	-0.014 ± 0.002	0.003 ± 0.000
Network variation	Mean flow	Max flow	Min flow	Volume
LPA	0.141 ± 0.001	0.447 ± 0.009	-0.001 ± 0.001	0.016 ± 0.000
RPA	0.027 ± 0.001	0.009 ± 0.010	-0.014 ± 0.004	0.003 ± 0.000

Values are expressed as means ± s.d. Pressure values are in units of mmHg, flow values are in units of cm^3/s, and volume values are in units of cm^3.

3.3 Forward UQ The MPA flow data is used as an inflow boundary condition, hence it does not change in any of the simulations. The ensemble averaged pressure predictions in the MPA, LPA, and RPA along with $\pm$ two standard deviations are shown in the first column of figure 9. Mean, systolic, diastolic and pulse pressure and max flow, min flow, and total volume, are given in table 2. The flow distribution to the LPA is much larger than the RPA, a consequence of the larger radius of the LPA that allows for greater fluid flow. This deviation in flow is apparent in the WI plots in figure 10, showing a more complex series of wave reflections in the RPA than the LPA and MPA. The ensemble averaged pressure waveform calculated from the 25 networks identifies the network generated by $(\theta_1,\theta_2) = (33, 5.1)$ as the representative network.

For the parameter variation component of the study, we use the inverse sampling methodology defined in §2.5.3 to propagate 10^4 realizations of perturbed radius and length values in the representative network. The second column of figure 9 shows the model predictions along with the mean and $\pm$ two standard deviations from the mean. The variation in the MPA, LPA, and RPA systolic and pulse pressure is significantly larger than the mean and diastolic pressures (see table 2). The flow predictions in the LPA and RPA have larger variability in mean and max flow in comparison to the minimum flow. The variation attributed to network size and connectivity is calculated by fixing each vessel's radius and length in the representative network before reducing the full network iteratively. As described in §2.5.4, we reduce the network by starting at the smallest branches and moving towards the proximal vasculature while ensuring that Windkessel boundary conditions are adjusted for each simulation (see figure 9). Overall, reducing the number of vessels from 219 in the largest network to 3 in smallest network introduces a discrepancy of approximately 10 mmHg in the pressure predictions of all three pulmonary arteries.

WI analysis results in figure 10 show that all vessels have two forward waves at the beginning and end of systole. The MPA and LPA have a pronounced backward wave during peak flow and the MPA and RPA have a secondary backward wave later in systole. The RPA also has an additional backward wave that occurs towards the end of diastole. The connectivity study in the last column of figure 10 shows that the MPA and LPA achieve their largest forward and backward WI value for the smallest network, while the opposite is true for the RPA. Time averaged PWV in the MPA, as calculated using equation (2.6), was 4.83 ± 0.0054 m/s for the total variation, 4.83 ± 0.0037 m/s for the parameter variation, and 4.84 ± 0.0054 m/s for the network variation. The mean PWV was 0.2% larger in the network variation study vs the total and parameter variation studies, a minimal relative difference.

4 Discussion

Recent advances in image segmentation have made subject-specific modelling of PH feasible, yet the modelling process still comprises segmentation induced uncertainty that propagates through to simulation results. This is the first known study to explicitly quantify the variability of 1D CFD blood flow and pressure predictions arising from uncertainty in pre-segmentation parameterization. We investigate three types of segmentation induced variations: the total variation arising from changes in pre-segmentation parameters, variation due to changes in vessel length and radius, and variation with respect to network connectivity and size. Results suggest that variation in network structure is the greater contributor to uncertainty in haemodynamic predictions, consistent with what is known of the pulmonary vascular physiology. Moreover, the methodology developed herein can be used to generate a 1D model network for any vascular system.

4.1 Segmentation and construction of network graphs

Results show that pre-segmentation parameters drastically influence the number of vessels in the network, while the number of generations attainable remains relatively consistent. It is apparent that the network obtained from image segmentation is strongly linked to the range of image intensities considered in the foreground via choice of (θ_1,θ_2). Most notably, the segmentation parameter set $(31, 6.1)$ gives a volume that is significantly smaller, suggesting that even slight changes in pre-segmentation parameters can reduce the number and size of small vessels captured. The largest vascular tree used in this study contains 500 vessels, a small fraction of the thousands of blood vessels that comprise the full pulmonary arterial system (4,9). We expect the trends seen in figure 5 to continue if more vessels are obtained from the segmentation. Our techniques study uncertainty induced by global thresholding, but could be applied when other pre-segmentation techniques are used, as global thresholding is commonly used (3,21,22) but is only one of many segmentation methods.

The variability in the total number of vessels for a given network highlights the variation attributed to segmentation. This would be expected in other networks that exhibit dispersive branching patterns, such as the coronary arteries (10) or cerebral vasculature (33). We employed a generation-based ordering scheme to describe the branching structure, where each bifurcation is considered a new generation of blood vessels. In contrast, other authors (42) have used other ordering systems, *e.g.*, Strahler (43) schemes, dentify structural properties of the pulmonary system, though these methods are not as compatible with CFD network models.

4.2 Inverse uncertainty quantification

KDEs and GPs are commonly used techniques (37,44) , but this study is the first to use GPs in density estimation for vascular measurements. Forward UQ is typically carried out by assuming a parametric

parameter distribution *a priori*, forcing prior assumptions on the unknown parameter distributions. By estimating the density directly from repeated measurements, we construct a nonparametric, representative density describing the uncertainty of the measurements across segmentations without prior assumptions.

The standardized measurements allow us to generalise the uncertainty of the 32-vessel subset to the entire vascular network, increasing the robustness of the density estimate. As shown in figure 8, the three density estimates are similar in the mode of the distribution (approximately zero); however the GP density estimation allows for additional UQ in both the density and CDF estimates (37). We construct marginal density estimates for the PDFs of radius and length, which assumes independence among the two quantities. PDF estimation methods that account for correlation between radius and length measurements should be investigated further.

GP regression is necessary for the data considered, as weighted least squares cannot correct the heteroscedastic variance. The coefficient of variation for the measurements increased as the measured dimensions decreased in value, suggesting that smaller vessels are subject to larger fluctuations in estimated dimensions when varying pre-segmentation parameters. The gradual increase in coefficient of variation indicates that the variance of the vessel dimensions across segmentations increases as vessels get smaller. Similar conclusions have been made in simulations predicting the fractional flow reserve in coronary crowns (10), as the smaller regions of the vasculature were susceptible to higher segmentation error. However, our work is the first to consider estimated, nonparametric densities for UQ propagation, and does not require *a priori* distribution assumptions.

4.3 Total variation of model simulations

The total network size obtained from the segmentation procedure has several effects on the model output. As shown in table 2, changes in network topology due to segmentation induced a variation in systolic pressure that was nearly 6 times larger than the variation of diastolic pressure. Moreover, we observe that the total variation for the systolic and pulse pressure is larger in comparison to the mean and diastolic pressure. All four of these pressure metrics are typically used in diagnostic tools of diseases such as PH (2). Though systolic pressure and pulse pressure have a small standard deviation (approximately 5% relative to the mean), studies investigating coronary related mortality found that these pressure quantities were important for risk assessment in patients with congenital heart disease (45). This further indicates a need for UQ when using these models for cardiovascular disease diagnostics and risk assessment.

4.4 Parameter variation

The standard deviation of diastolic pressure resulting from parameter (radius and length) variation is greater than that resulting from network (size and connectivity) variation. This suggests that changes in vessel dimensions and nominal boundary conditions can ultimately raise the diastolic pressure of the

system, which is expected in the case of chronic vascular remodelling (2). Parameter variation only accounted for approximately 30% of the total variation in the pulse pressure and had less of an effect on all other pressure and flow quantities when compared to the network variation. Larger networks encompassing the entire pulmonary tree will increase the parameter uncertainty, as they correspond to more vessels and more uncertain estimates of radius and length. This would in turn bias haemodynamic parameter estimates, since network predictions would be based on the initial segmentation results (14).

4.5 Network variation

The largest effects on pressure and flow waveform predictions in the network are attributed to changes in network connectivity and size, as seen in figures 9 and 10. Quantitative metrics provided in table 2 also show that network variation produces larger standard deviations in systolic and pulse pressures vs parameter variation, suggesting that the configuration of vessels in the pulmonary system may play an important role in haemodynamic predictions. It is known that the highly compliant pulmonary system utilizes its rapidly branching structure to perfuse the lung under a low-pressure gradient and varying cardiac outputs, and that network remodeling is common with pulmonary vascular disease (2,4). For example, Rol et. al (42) concluded that changes in vessel diameter with PH cannot solely explain the increase in vascular resistance, and further hypothesized that network rarefaction may be a larger contributor to increased pulmonary arterial pressure. Olufsen et. al (25) investigated this computationally by altering structured tree boundary conditions, effectively reducing the size of the microvasculature and increasing pulmonary artery pressure. Our model analysis agrees with clinical hypotheses that vascular rarefaction and associated changes in network size and connectivity contribute more to changes in pulmonary arterial pressure than vessel narrowing.

The Poiseuille relation used to distribute network resistance introduces an impedance mismatch at each terminal vessel. Reflected pressure waves due to this mismatch become more prevalent as successive vessels are added to the system, leading to an increased pressure (16,48). While other studies have considered non-reflective boundary conditions (15,46), it is hypothesised that wave reflections occur in the pulmonary system when PH is present (49), illustrating the appropriateness of reflective boundary conditions in the model.

Our results show three instances where reducing part of the network causes a larger change in pressure, which agree with a previous investigation by Epstein *et al.* (46) that showed a critical threshold in the number of vessels that lead to larger discrepancy in haemodynamic predictions. It is often the case that haemodynamic data is only available in select locations of the vascular system (3,29,30). Changes in network size will lead to changes in optimal parameter values during parameter inference, making the problem ill-posed as estimated parameters describing stiffness, compliance, and vascular resistance will depend on the size of the network used in CFD simulations. This further indicates that uncertainty in the

network structure must be taken into account when using 1D CFD models for clinical decision making (30).

4.6 Limitations and future directions

Several potential limitations of this study can be addressed in future investigations. First, we assume negligible tapering in each vessel, which could play a role in proximal artery dynamics. Second, our model assumptions ignore radius dependent stiffness and the effects of wall-viscoelasticity, which may be important in pulmonary arteries (48) and could change the model sensitivity to network size and vessel dimensions. However, the focus of this study was to quantify how changes in the model domain attributed to pre-segmentation parameters impact haemodynamic predictions for fixed material parameters. Similar to previous studies (29,30,33), nominal parameters are calculated under the assumption of steady flow and that pressure does not drop in the large vessels. However, in the 1D domain we solve non-linear equations, which account for inertial and viscous losses resulting in a pressure drop along the vessels. Similar to the systemic circulation, we assume a negligible pressure drop along the large pulmonary vessels. Yet no experimental studies have measured pressure beyond the first few generations, hence validation of this assumption in the pulmonary circulation is difficult

Additional limitations involved model construction and quantified results. The length of the smallest vessels was augmented during simulations to ensure the CFL condition is not violated. The CFL condition could also be met by either increasing the number of time-steps, which increases computational cost, or devising a numerical scheme using adaptive time-stepping, extending the scope of the study. We also provided conventional mean and standard deviation calculations as familiar metrics for comparison. An alternative approach is to perform formal global sensitivity analysis. State-of-the-art methods are based on Sobol indices defined via conditional variances of different order (13,14,30,42); however, their computation via Monte Carlo or quasi-Monte Carlo simulations is computationally expensive. This computational complexity is aggravated by the fact that the image segmentation includes manual inspection and the parameter space can therefore only be sampled at a coarse level. A potential way to alleviate this problem is to use statistical emulation, e.g. using GPs, to compute first order and total effects indices. This can, in principle, follow the method described in (42), by adapting and extending existing approaches and software tools; see https://github.com/samcoveney/maGPy . However, this exploration is beyond the scope of the present study and provides an interesting direction for future research.

We consider the frequently-used three-element Windkessel model as the boundary condition for the 1D model, yet this model greatly simplifies the physiological resistance beyond the segmented vessels. In contrast, structured tree boundary conditions (24,25,28) can provide an additional level of

complexity for approximating downstream resistance and attempt to capture network structure beyond the limits of image segmentation. In addition, the experimental protocol inhibited the same mouse from being used for both the haemodynamic and imaging data. While this is a limitation for possible parameter inference, our methodology still captures variability in model predictions due to uncertainty in the vessel dimensions and network structure. Future human-based studies could incorporate non-invasive flow and imaging data from the same patient in the model. Finally, future subject-specific models of the pulmonary vasculature would be enhanced by allowing for trifurcations and considering branching angles in the vascular tree, thus accounting for more of the physiological traits of the network.

5 Conclusions

Uncertainty of model predictions must be accounted for in the absence of ground truth. We have presented the first known investigation of the impact of uncertainties in imaging-based network reconstruction on CFD simulations in the pulmonary vasculature. This work identifies the uncertainties pertaining to image pre-segmentation parameters by explicitly measuring the variation in radius and length measurements of a subset of vascular segments. Another novelty of this work is in estimating densities of radius and length from data obtained using state-of-the-art nonparametric techniques, rather than assuming a fixed and potentially biased functional form of the distribution *a priori*. Moreover, our study is the first to perform UQ on the dimensions and network topology of a 1D CFD model in an expansive pulmonary vascular network. Our results show that the network variation has the most influence on predictions of blood pressure and flow while changes in vessel length and radius have less impact on haemodynamic predictions.

Author contributions

M.J.C. designed the study, developed algorithms, performed all haemodynamic simulations, pre- and post-processeing of data, and drafted the manuscript. M.L.P. and D.H. carried out statistical analyses with GPs and helped revise the manuscript. N.C. designed the experimental protocol and gave clinical insight. M.U.Q., M.S.O and L.E.F conceived and coordinated the study and helped with revisions of the manuscript. All authors gave final approval for publication.

Acknowledgements

We thank Dr. Diana Tabima for her review and input on the experimental protocol.

Data accessibility

Data accessibility. The datasets supporting this article have been uploaded as part of the electronic supplementary material. Software/code implementing the developed methodology can be found at https://github.com/mjcolebank.

Funding

This work was supported by the NSF-DMS (1246991 and 1615820), the EPSRC (EP/N014642/1), the Royal Society of Edinburgh (62335), the NIH (R01 HL-086939), and the American Heart Foundation (19PRE34380459).

Competing interests

We have no competing interests.

References

1. Lang IM, Plank C, Sadushi-Kolici R, Jakowitsch J, Klepetko W, Maurer G. (2010) Imaging in pulmonary hypertension. JACC Cardiovasc Imaging, 3:1287-95
2. Fukumoto Y. (2015) Diagnosis and treatment of pulmonary hypertension. Singapore: Springer, 101:311-19
3. Qureshi MU, Colebank MJ, Paun M, Ellwein L, Chesler N, Haider MA, Hill NA, Husmeier D, Olufsen MS. (2019) Hemodynamic assessment of pulmonary hypertension in mice: a model based analysis of the disease mechanism. Biomech Model Mechanobiol, 18:219-43
4. Tawhai MH, Clark AR, Burrowes KS. (2011) Computational Models of the Pulmonary Circulation. Pulm Circ, 1:224-38
5. Davidoiu V, Hadjilucas L, Teh I, Smith NP, Schneider JE, Lee J. (2016) Evaluation of noise removal algorithms for imaging and reconstruction of vascular networks using micro-CT. Biomed Phys Eng Express, 2:045015
6. Antiga L, Piccinelli M, Botti L, Ene-Iordache B, Remuzzi A, Steinman DA. (2008) An image-based modeling framework for patient-specific computational haemodynamics. Med Biol Eng Comput, 46:1097-112
7. Payer C, Pienn M, Bálint Z, Shekhovtsov A, Talakic E, Nagy E, Olschewski A, Olschewski H, Uschler M. (2016) Automated integer programming based separation of arteries and veins from thoracic CT images. Med Image Anal, 34:109-22.
8. Van Rikxoort EM, Van Ginneken B. (2013) Automated segmentation of pulmonary structures in thoracic computed tomography scans. Phys Med Biol, 58:R187-220
9. Helmberger M, Pienn M, Urschler M, Kullnig P, Stollberger R, Kovacs G, Olschewski A, Olschewski H, Bálint Z. (2014) Quantification of tortuosity and fractal dimension of the lung vessels in pulmonary hypertension patients. PLoS One, 9:e87515
10. van Horssen P, van Lier MG, van den Wijngaard JP, VanBavel E, Hoefer IE, Spaan JA, Siebes M. (2016) Influence of segmented vessel size due to limited imaging resolution on coronary hyperemic flow prediction from arterial crown volume. Am J Physiol, 310:H839-46
11. Rempfler M, Andres B, Menze BH. (2017) Uncertainty Estimation in Vascular Networks. Lec Notes Comp Sci, 10551:42-52
12. Kheyfets VO, Rios L, Smith T, Schroeder T, Mueller J, Murali S, Lasorda D, Zikos A, Spotti J, Reilly JJ Jr, Finol EA. (2015) Patient-specific computational modeling of blood flow in the pulmonary arterial circulation. Comput Methods Programs Biomed, 120:88-101
13. Huberts W, Donders WP, Delhaas T, van de Vosse FN. (2014) Applicability of the polynomial chaos expansion method for personalization of a cardiovascular pulse wave propagation model. Int

J Numer Meth Biomed Eng, 30:1679-704

14. Sankaran S, Grady L, Taylor CA. (2015) Fast computation of haemodynamic sensitivity to lumen segmentation uncertainty. IEEE Trans Med Imaging, 34:2562-71
15. Alastruey J, Xiao N, Fok H, Schaeffter T, Figueroa CA. (2016) On the impact of modelling assumptions in multi-scale, subject-specific models of aortic haemodynamics. J R Soc Interface, 13:20160073
16. Rivolo S, Hadjilucas L, Sinclair M, van Horssen P, van den Wijngaard J, Wesolowski R, Chiribi A, Siebes M, Smith NP, Lee J. (2016) Impact of coronary bifurcation morphology on wave propagation. Am J Physiol, 311:H855-70
17. Fossan FE, Mariscal-Harana J, Alastruey J, Hellevik LR. (2018) Optimization of topological complexity for one-dimensional arterial blood flow models. J R Soc Interface, 15:20180546
18. Vanderpool RR, Kim AR, Molthen RC, Chesler NC. (2010) Effects of acute Rho kinase inhibition on chronic hypoxia-induced changes in proximal and distal pulmonary arterial structure and function. J Appl Physiol, 1609:188-98
19. Tabima DM, Roldan-Alzate A, Wang Z, Hacker TA, Molthen RC, Chesler NC. (2012) Persistent vascular collagen accumulation alters haemodynamic recovery from chronic hypoxia. J Biomech, 45:799-804
20. Yushkevich PA, Piven J, Hazlett HC, Smith RG, Ho S, Gee JC, Gerig G. (2006) User-guided 3D active contour segmentation of anatomical structures: Significantly improved efficiency and reliability. Neuroimage, 31:1116-28
21. Newberry MG, Ennis DB, Savage VM. (2015) Testing foundations of biological scaling theory using automated measurements of vascular networks. PLoS Comput Biol, 11:1-18
22. Ellwein LM, Marks DS, Migrino RQ, Foley WD, Sherman S, LaDisa JF. (2016) Image-based quantification of 3D morphology for bifurcations in the left coronary artery. Catheter Cardiovasc Interv, 87:1244-55
23. Utkarsh A. (2015) The Paraview Guide: A Parallel Visualization Application. Clifton Park, NY: Kitware, Inc.
24. Olufsen MS, Peskin CS, Kim WY, Pedersen EM, Nadim A, Larsen J. (2000) Numerical simulation and experimental validation of blood flow in arteries with structured-tree outflow conditions. Ann Biomed Eng, 28:1281-99
25. Olufsen MS, Hill NA, Vaughan GDA, Sainsbury C, Johnson M. (2012) Rarefaction and blood pressure in systemic and pulmonary arteries. J Fluid Mech, 705:280-305
26. Riches AC, Sharp JG, Thomas DB, Smith SV. (1973) Blood volume determination in the mouse. J Physiol, 228:279-84

27. Windberger U, Bartholovitsch A, Plasenzetti R, Korak KJ, Heinze G. (2003) Whole blood viscosity, plasma viscosity and erythrocyte aggregation in nine mammalian species. Exp Physiol, 88:431-40
28. Qureshi MU, Vaughan GDA, Sainsbury C, Johnson M, Peskin CS, Olufsen MS, Hill NA. (2014) Numerical simulation of blood flow and pressure drop in the pulmonary arterial and venous circulation. Biomech Model Mechanobiol, 13:1137-54
29. Paun LM, Qureshi MU, Colebank MJ, Hill NA, Olufsen MS, Haider MA, Husmeier D. (2018) MCMC methods for inference in a mathematical model of pulmonary circulation. Stat Neerl, 72:306-38
30. Colebank MJ, Qureshi MU, Olufsen MS. (2019) Sensitivity analysis and uncertainty quantification of 1D models of the pulmonary hemodynamics in mice under control and hypertensive conditions. Int J Numer Meth Biomed Eng, e3242.
31. Su J, Hilberg O, Howard L, Simonsen U, Hughes AD. (2016) A review of wave mechanics in the pulmonary artery with an emphasis on wave intensity analysis. Acta Physiol. 218:239-49
32. Hughes AD, Parker KH. (2009) Forward and backward waves in the arterial system. Med Biol Eng Comput. 47:207-10
33. Reymond P, Merenda F, Perren F, Ru D. (2009) Validation of a one-dimensional model of the systemic arterial tree. Am J Physiol, 297:208-22.
34. Krenz GS, Dawson CA. (2003) Flow and pressure distributions in vascular networks consisting of distensible vessels. Am J Physiol, 284:H2192-203.
35. Silverman BW. (1998) Density Estimation for Statistics and Data Analysis. Boca Raton, FL: Chapman & Hall/CRC Press.
36. Guidoum, A.C. (2015) kedd: Kernel estimator and bandwidth selection for density and its derivatives. R package version 1.0.3. http://CRAN.R-project.org/package=kedd (accessed August 2018).
37. Riihimäki J, Vehtari A. (2014) Laplace approximation for logistic gaussian process density estimation and regression. Bayesian Anal, 9:425-48
38. Vanhatalo J, Riihimäki J, Hartikainen J, Jylänki P, Tolvanen V, Vehtari A. (2013) GPstuff: Bayesian Modeling with Gaussian Processes. J Mach Learn Res, 14:1175-9
39. Goldberg P, Williams C, Bishop C. (1997) Regression with input-dependent noise. Adv Neural Inf Process Syst. 10:493-9
40. Hastie T, Tibshirani R, Friedman J. (2009) The Elements of Statistical Learning: Data Mining, Inference, and Prediction. New York, NY; Springer.
41. Rasmussen CE, Williams CKI. (2006) Gaussian processes for machine learning. The MIT Press.

42. Huang W, Yen RT, McLaurine M, Bledsoe G. (1996) Morphometry of the human pulmonary vasculature. J Appl Physiol, 81:2123-33

43. Rol N, Timmer EM, Faes TJC, Noordegraaf AV, Grünberg K, Bogaard HJ, Westerhof N. (2017) Vascular narrowing in pulmonary arterial hypertension is heterogeneous: rethinking resistance. Physiol Rep, 5:1-9.

44. Melis A, Clayton RH, Marzo A. (2017) Bayesian sensitivity analysis of a 1D vascular model with Gaussian process emulators. Int J Numer Meth Biomed Eng, 33:1-11

45. Kind T, Faes TJC, Vonk-Noordegraaf A, Westerhof N. (2011) Proportional relations between systolic, diastolic and mean pulmonary artery pressure are explained by vascular properties. Cardiovasc Eng Technol, 2:15-23.

46. Epstein S, Willemet M, Chowienczyk PJ, Alastruey J. (2015) Reducing the number of parameters in 1D arterial blood flow modeling. Am J Physiol, 309:H222-34.

47. Gounley J, Vardhan M, Randles A. (2017) A computational framework to assess the influence of changes in vascular geometry on blood flow. Proc Platf Adv Sci Comput Conf, 2:1-8

48. Wang Z, Lakes RS, Golob M, Eickhoff JC, Chesler NC. (2013) Changes in large pulmonary arterial viscoelasticity in chronic pulmonary hypertension. PLoS One. 8: e78569.

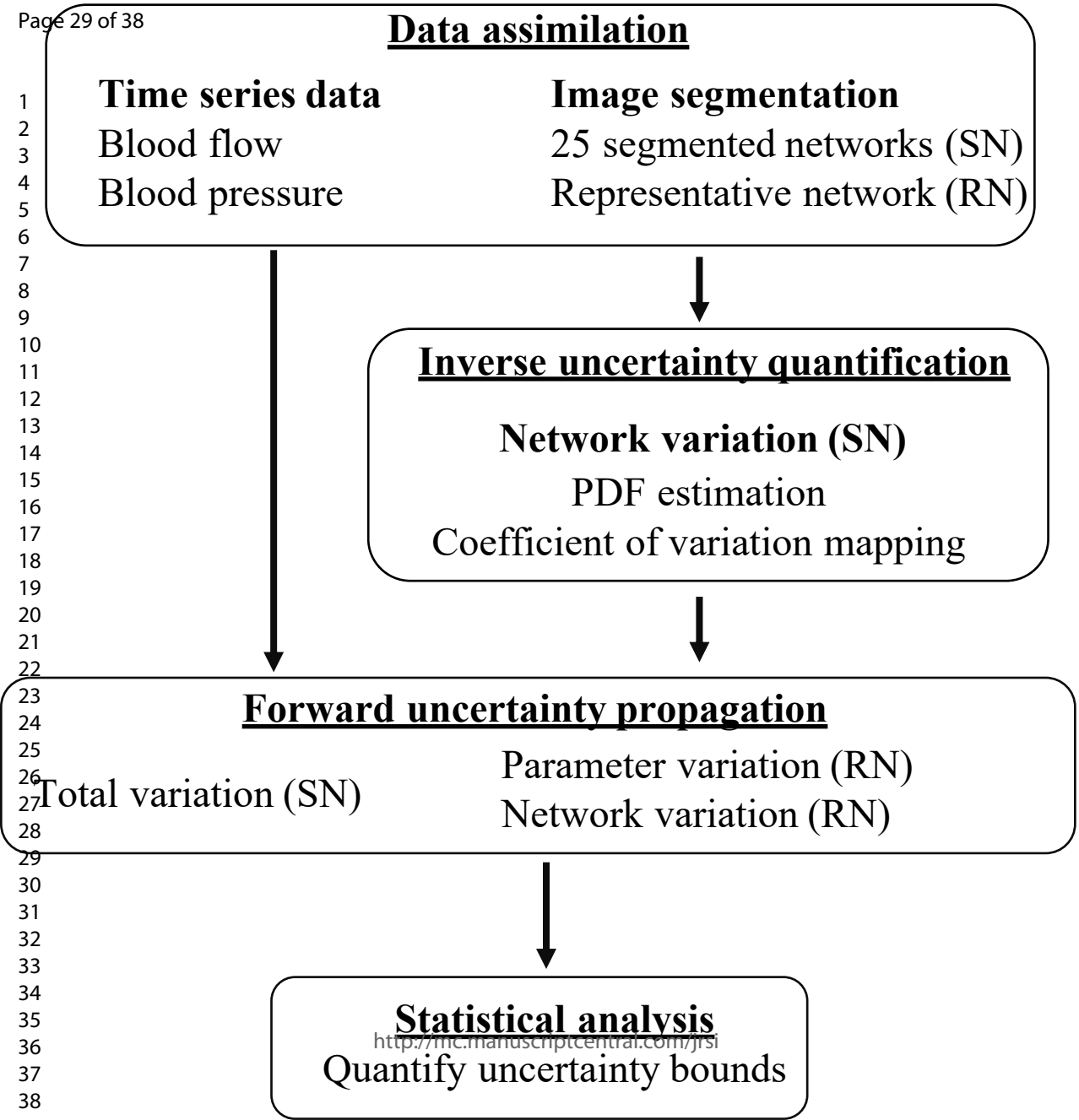

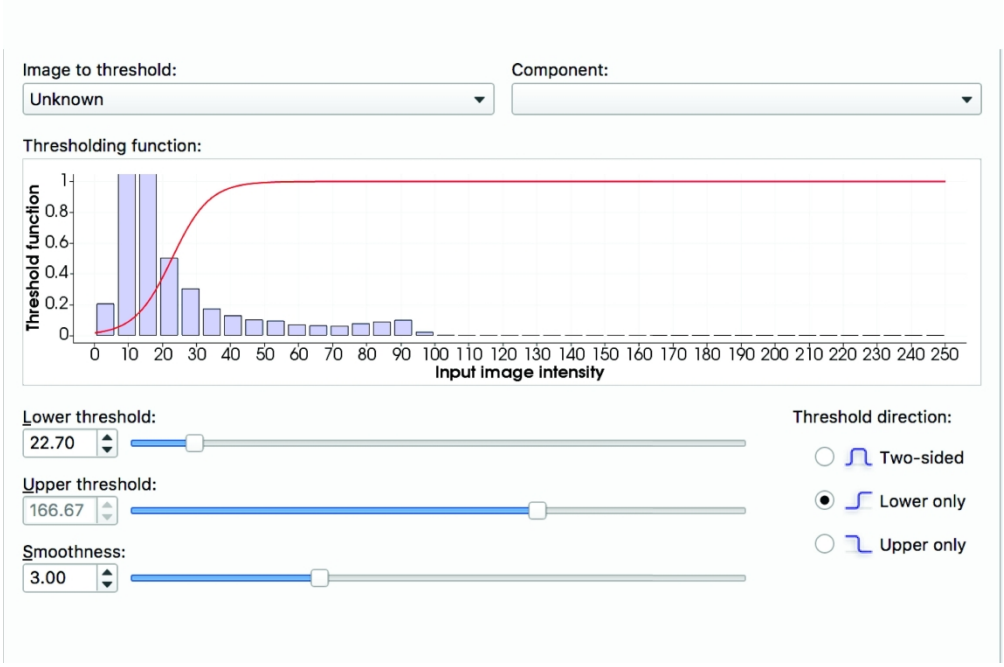

Figure 2: ITK-SNAP interface for prescribing (θ_1,θ_2). Voxel intensities in the histogram are mapped to foreground and background based on thresholding function (red curve) and pre-segmentation parameters. Here, we only assume a lower threshold on image intensities, as shown by the constant value of 1 in the threshold function for all values greater than the lower threshold.

251x166mm (300 x 300 DPI)

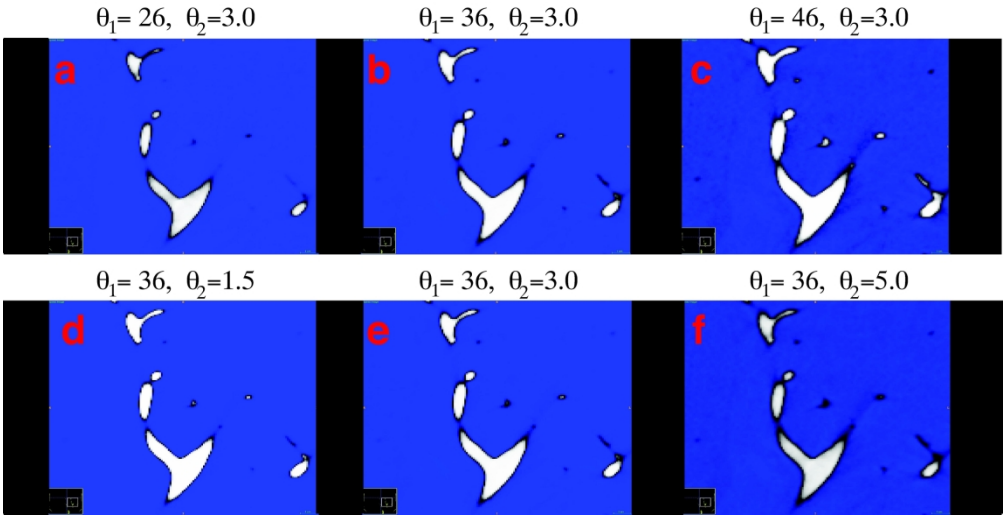

Figure 3: Qualitative differences in foreground (white) of distal vascular segments when changing the lower threshold (θ_1) and the smoothing parameter (θ_2). Top: changes in foreground with θ_1; bottom: changes in foreground with θ_2.

260x133mm (300 x 300 DPI)

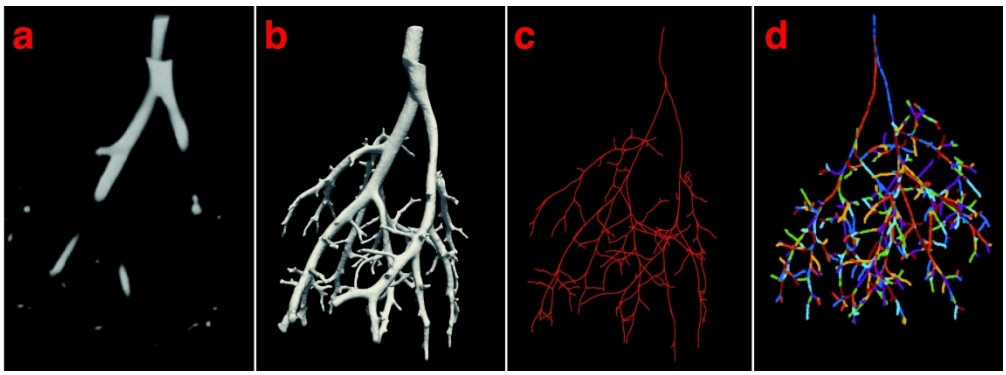

Figure 4: Image to network workflow. a) the foreground visible in the image file; b) the 3D rendering of the vascular foreground; c) centerlines obtained using VMTK; d) a graph representation of the network used in the 1D model with vessels (edges) and bifurcations (nodes) identified using custom MATLAB algorithms.

324x118mm (300 x 300 DPI)

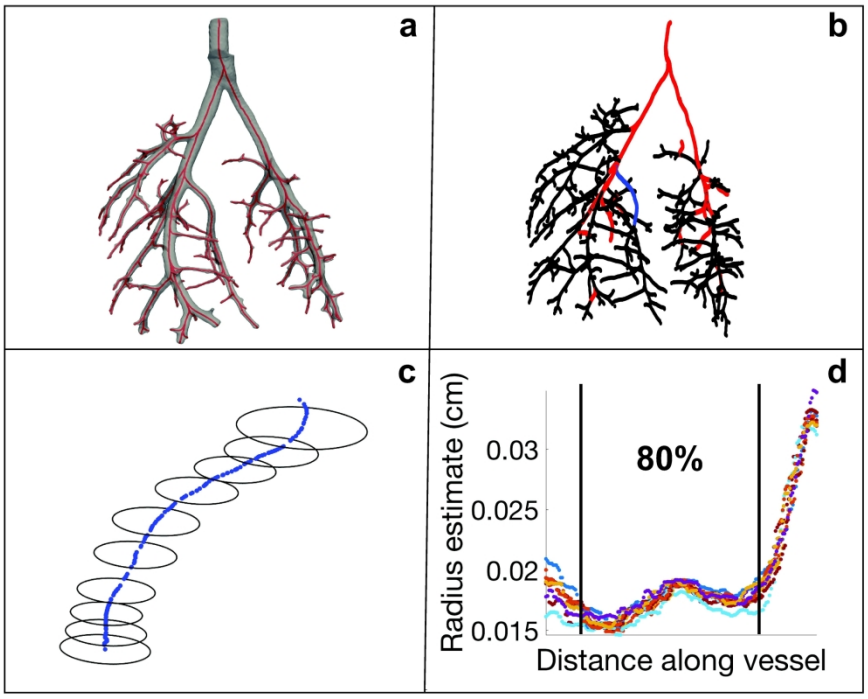

Figure 5: Components of an arterial tree. a) 3D segmentation of network; b) centerline representation of a tree with the 32 vessel-subset (red and blue); c) magnification of the representative vessel in blue from panel (b) depicting radius estimates; d) radius estimates along the representative vessel in panel (c), where the center 80% of points are used to calculate the mean radius. Actual radius values obtained in (d) are calculated at orthogonal centerline slices in VMTK, while panel (c) shows non-orthogonal radii estimates for illustrative purposes.

249x196mm (300 x 300 DPI)

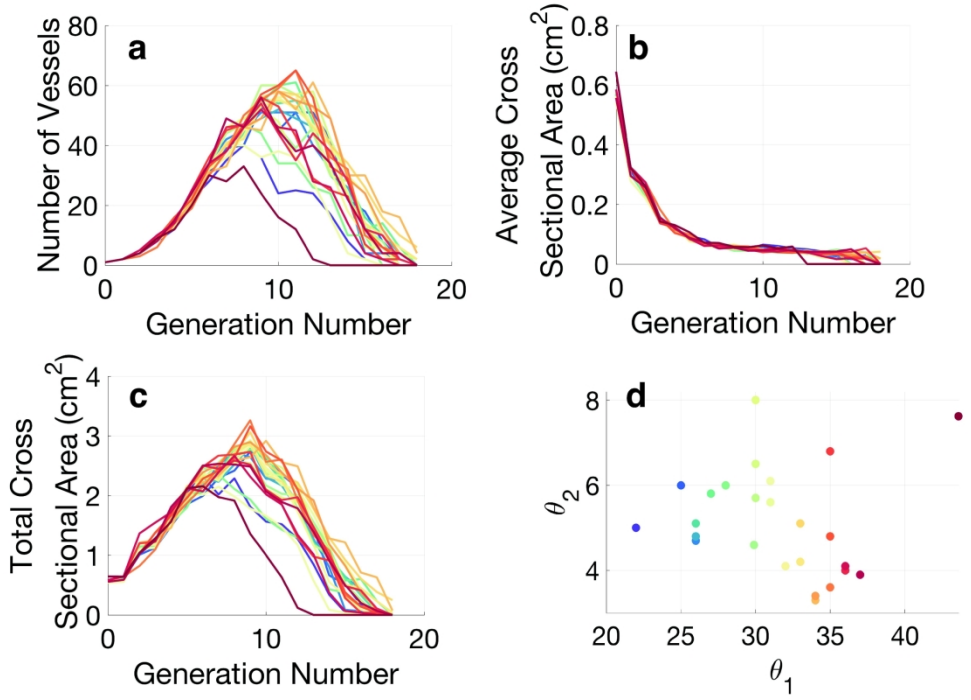

Figure 6: Morphometric features from the 25 segmentations marked by different colored lines. The number of vessels (a) is consistent between segmentations until the 5th generation. The average cross-sectional area (b) decreases rapidly after the 1st generation, while the total cross-sectional area (c) varies significantly between segmentations. The segmentation parameters are plotted against each other in (d), with a clear outlier present at (44,7.6) (in pink) indicating a set of pre-segmentation parameters that have marked effects on the network structure. The outlier has lower number of vessels and total cross-sectional area as depicted in the pink curve in panels (a) and (c).

245x171mm (300 x 300 DPI)

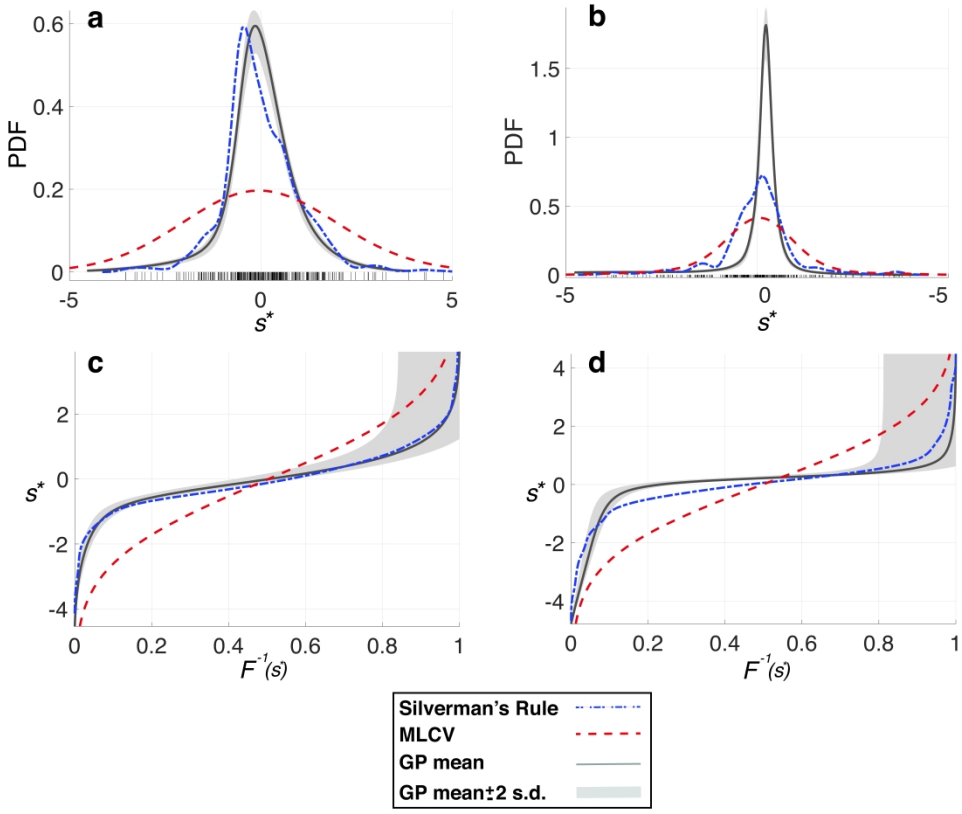

Figure 7: Density estimates (a) and (b) and inverse cumulative distribution functions (c) and (d) for the standardized radius and length values, respectively, measured in the 32-vessel subset. The bandwidth parameters used for the length and radius KDEs were determined using Silverman's rule (blue, dash dot) and maximum likelihood cross-validation (MLCV, red, dashed). The Gaussian process (GP) mean and 95% confidence interval are shown as a solid curve with grey bands. Standardized values are denoted by the black tick marks in panels (a) and (b).

639x531mm (600 x 600 DPI)

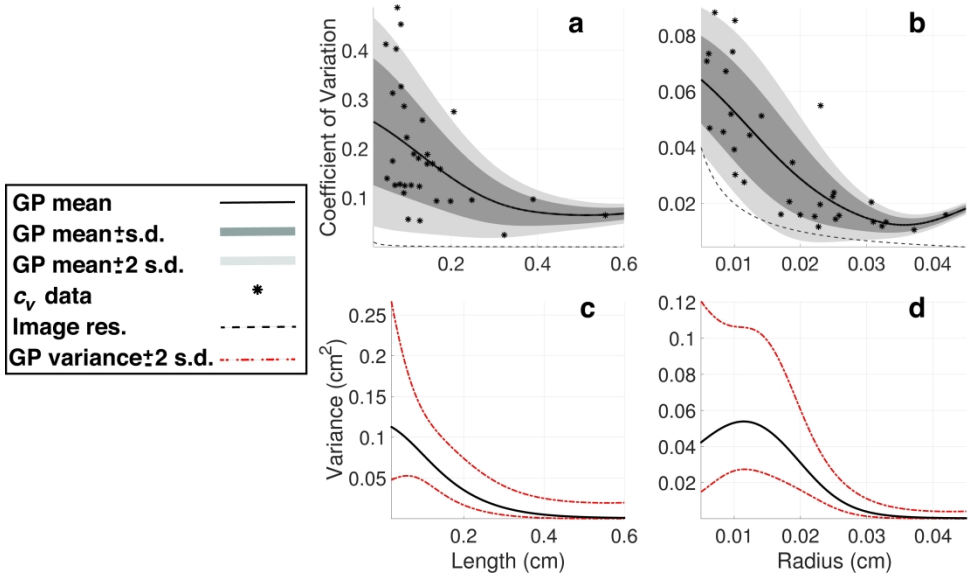

Figure 8: Gaussian Process (GP) regression using non-constant variance for the relationship between length and radius and their coefficient of variation (c_v). The GP means and standard deviations are computed from the c_v data obtained from the 32-vessel subset (asterisks) and plotted against the analytical bound of the image resolution (blue, dash-dot curve). The mean of the GPs and ± one and two standard deviations (SD) from the mean are shown in (a) and (b) in black, dark grey, and light grey, respectively. The variance of the GPs in (c) and (d) are predicted using an additional GP and provide a mean (black) and variance (dashed curve) for the variance estimate. Both mean curves in (a) and (b) are above the uncertainty bound of the imaging protocol.

548x328mm (300 x 300 DPI)

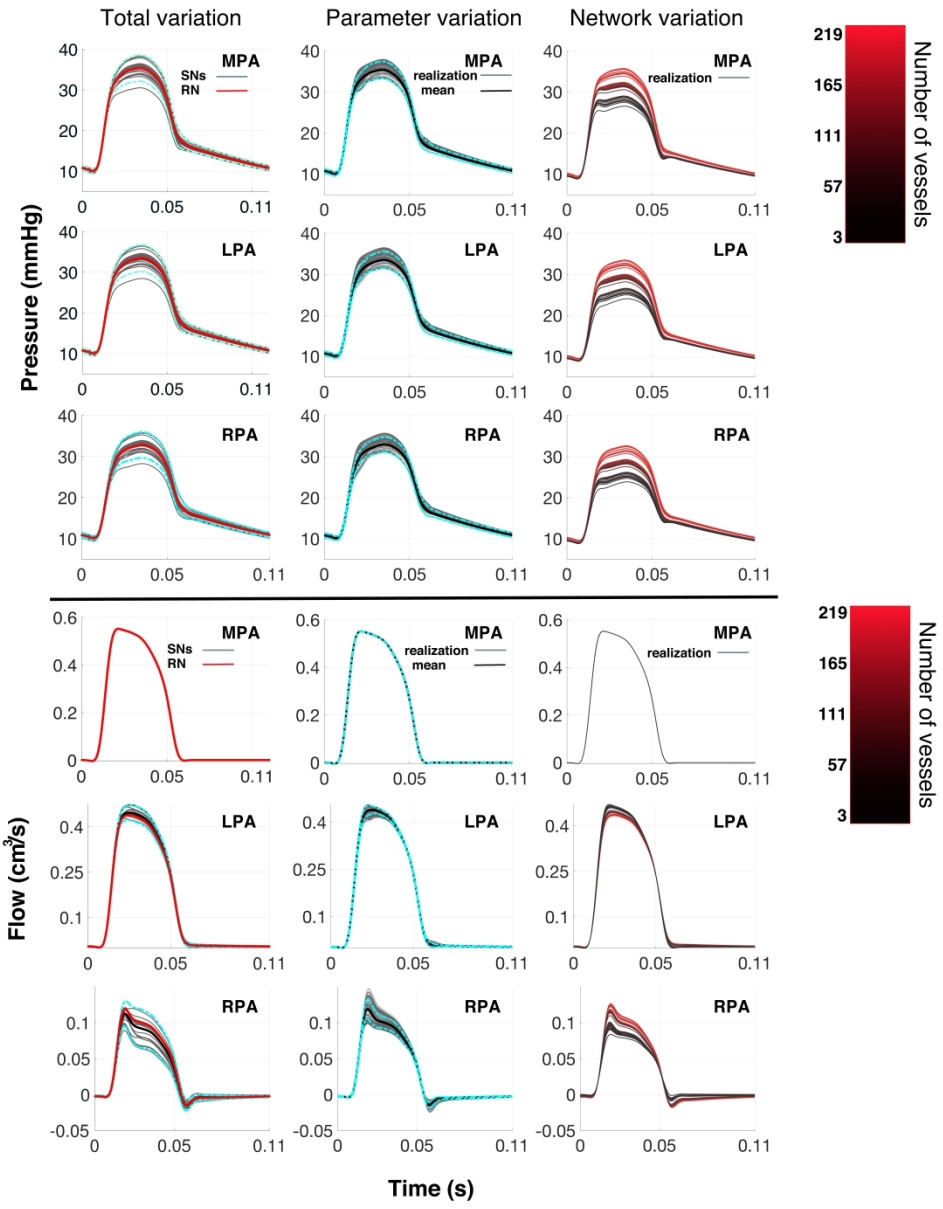

Figure 9. Pressure and flow predictions in the first pulmonary bifurcation when studying total variation, parameter variation, and network variation. Predictions from the total variation include simulations in the 25 segmented networks, the representative network (in red), and ±2 s.d. from the mean (blue, dash-dot). The parameter variation plots (2nd column) show the 10,000 Monte Carlo realizations (grey) along with the mean (black) ±2 s.d. from the mean (blue, dash-dot). Lastly, the network variation predictions (3rd column) show the predictions when using 219 vessels in the network (bright red) up until the network is reduced to the MPA, LPA, and RPA (black).

763x975mm (600 x 600 DPI)

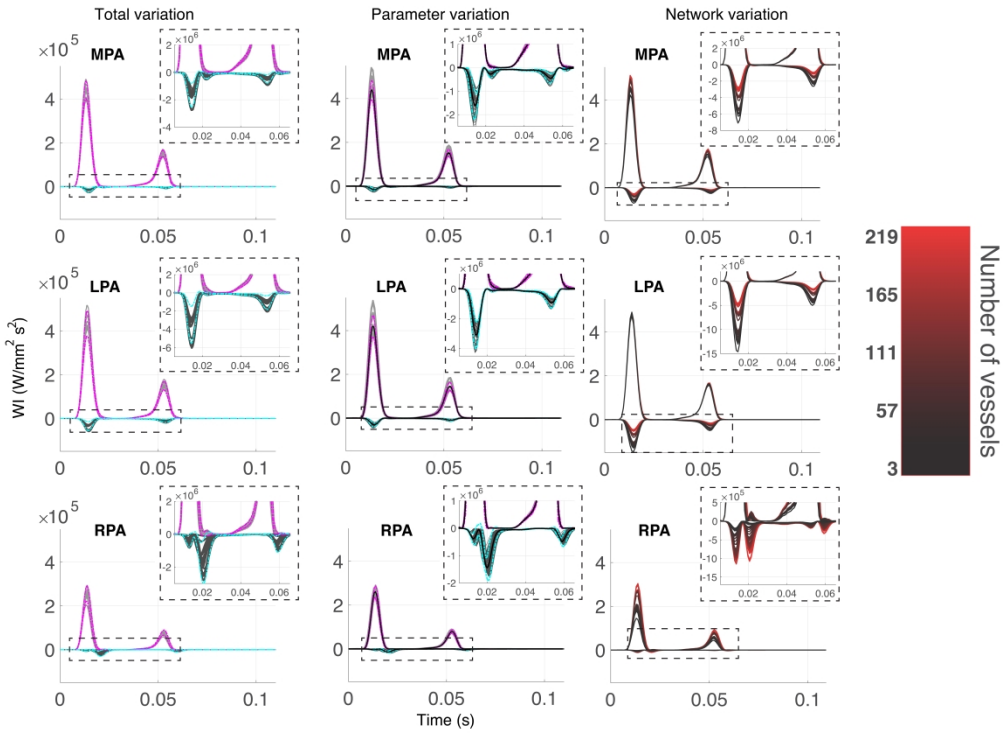

Figure 10. Wave intensity (WI) analysis in the first pulmonary bifurcation. Forward (positive values) and backward (negative values) waves are calculated for the total variation and parameter variation (grey lines) along with ±2 s.d. from the mean (forward waves, magenta; backward waves, cyan). Predictions from the network variation study are color coded according to network size, as described in Figure 9.

711x516mm (600 x 600 DPI)